Filament stitching

An architected printing strategy to mitigate anisotropy in 3D-Printed engineered cementitious composites (ECC)

Zhou, Wen; Xu, Yading; Meng, Zhaozheng; Xie, Jinbao; Zhou, Yubao; Schlangen, Erik; Šavija, Branko

DOI
10.1016/j.cemconcomp.2025.106044

Publication date
2025

Document Version
Final published version

Published in
Cement and Concrete Composites

Citation (APA)
Zhou, W., Xu, Y., Meng, Z., Xie, J., Zhou, Y., Schlangen, E., & Šavija, B. (2025). Filament stitching: An architected printing strategy to mitigate anisotropy in 3D-Printed engineered cementitious composites (ECC). *Cement and Concrete Composites*, *160*, Article 106044. https://doi.org/10.1016/j.cemconcomp.2025.106044

Cement and Concrete Composites 160 (2025) 106044

Contents lists available at ScienceDirect

Cement and Concrete Composites

journal homepage: www.elsevier.com/locate/cemconcomp

Filament stitching: An architected printing strategy to mitigate anisotropy in 3D-Printed engineered cementitious composites (ECC)

Wen Zhou [*], Yading Xu, Zhaozheng Meng, Jinbao Xie, Yubao Zhou, Erik Schlangen, Branko Šavija

Faculty of Civil Engineering and Geosciences, Delft University of Technology, Stevinweg 1, 2628 CN, Delft, the Netherlands

ARTICLE INFO

Keywords:
3D printing
Engineered cementitious composites (ECC)
Anisotropy
Architected structure
Flexural properties

ABSTRACT

Anisotropy in 3D-printed concrete structures has persistently raised concerns regarding structural integrity and safety. In this study, an architected 3D printing strategy, "stitching", was proposed to mitigate anisotropy in 3D-printed Engineered Cementitious Composites (ECC). This approach integrates the direction-dependent tensile resistance of extruded ECC, the mechanical interlocking between three-dimensional layers, and a deliberately engineered interwoven interface system. As a result, the out-of-plane direction of the printed structure can be self-reinforced without external reinforcements. Four-point bending tests demonstrated that the "stitching" pattern induced multi-cracking and flexural-hardening behavior in the out-of-plane direction, boosting its energy dissipation to 343 % of the reference "parallel" printing and achieving 48.6 % of cast ECC. Additionally, micro-CT scanning and acoustic emission tests further validated the controlled crack propagation enabled by the engineered interface architecture. The proposed strategy has been proven to substantially alleviate anisotropy and enhance structural integrity.

1. Introduction

Additive manufacturing of concrete, commonly known as 3D printing (3DP) of concrete, has emerged as a revolutionary technology in the construction industry [1–5]. Nevertheless, this layer-by-layer fabrication process presents inherent challenges: the interfaces between printed filaments and layers introduce discontinuities in material properties due to factors such as trapped air voids, rapid structuration and high thixotropy of the material, long cycling time, and moisture loss at the surface [6–12]. These discontinuities give rise to anisotropic behavior, which can undermine the structural integrity and overall performance of printed structures.

Anisotropy in 3D-printed structures is widely reported, with mechanical properties varying considerably with sampling and loading orientations [13–16]. For instance, in the traditional parallel printing pattern (Fig. 1), flexural and tensile properties are most favorable in the in-plane directions, Orientations 1 and 2. However, Orientation 3 often exhibits compromised performance due to the presence of layer interfaces [16]. Consequently, tensile or flexural properties in this vertical orientation are typically the weakest, resulting in a notable directional variation in structural performance. While less extensively studied, Orientation 4 also demonstrates inferior mechanical properties compared to Orientations 1 and 2 as more inter-filament interfaces are involved [17,18].

In fiber-reinforced cementitious materials, such as Fiber-Reinforced Concrete (FRC) or Engineered Cementitious Composites (ECC), the anisotropy is even more pronounced [19–21]. Fiber alignment during extrusion enhances mechanical properties in the in-plane directions (Orientations 1 and 2), often comparable to or outperforming their cast counterparts [22–28]. However, anisotropy persists, especially in Orientation 3, where the lack of fiber bridging at the interfaces weakens the bonding [29,30]. Studies have shown reductions of up to 90 % in flexural strength when switching from Orientation 1 to Orientation 3 [27,31,32].

A variety of reinforcing strategies have been explored to mitigate anisotropy [33–38]. A non-exhaustive list of these approaches includes:

(1) *Embedded reinforcements in the vertical direction.* One of the most commonly used and straightforward methods involves embedding external reinforcements, such as steel rebars [39–44],

* Corresponding author.
E-mail addresses: w.zhou-2@tudelft.nl (W. Zhou), yadingx@gmail.com (Y. Xu), z.meng@tudelft.nl (Z. Meng), j.xie-1@tudelft.nl (J. Xie), y.zhou-16@tudelft.nl (Y. Zhou), Erik.Schlangen@tudelft.nl (E. Schlangen), b.savija@tudelft.nl (B. Šavija).

https://doi.org/10.1016/j.cemconcomp.2025.106044
Received 27 January 2025; Received in revised form 27 February 2025; Accepted 12 March 2025
Available online 18 March 2025

mesh/textile [45–47], and pin/staple/U-nail [48–51], perpendicular to the printing plane to provide enhanced cross-layer support. These reinforcements can be manually placed or automatically inserted.

(2) *Bonding agent/layer at the interface.* Adhesive agents such as cement paste/mortar [52,53], epoxy/polymer-based composites [54–56], and fiber-reinforced cementitious composites [57] are applied to the surface of freshly printed layers to promote interlayer bonding.

(3) *Mechanical interlocking.* This method involves integrating surface features such as tongue-and-groove geometry or modifying the surface roughness of printed layers to facilitate better adhesion with subsequent layers [26].

(4) *Post-installed reinforcements.* In this approach, external reinforcements, e.g., prestressed steel cables, are installed after the printing and hardening of concrete components to enhance structural performance [58–61]. This method is commonly applied when assembling multiple printed elements, where reinforcements connect the components to form larger structures, such as bridges [62].

While these techniques offer feasible solutions for strengthening Orientation 3, their effectiveness and level of automation vary considerably. Although all methods succeed in increasing interlayer bonding strength, most offer limited improvements in ductility, if any. This raises concerns about brittle failure at interfaces and potential threats to structural integrity and safety. In Method (1), ductile behavior in the out-of-plane direction is possible but not always guaranteed, as it highly depends on the type, quantity, and arrangement of the reinforcements. Additionally, challenges persist regarding the continuity of reinforcements across interfaces, as well as bonding quality and long-term durability [63,64]. Methods (2) and (3), which utilize bonding layers or surface modification, enhance surface bonding between layer; however, the overall structure still requires extra reinforcement, such as steel rebars, for structural strengthening. Pre-installed reinforcement, as implemented in Method (4), offers the greatest potential to achieve ductile behavior comparable to reinforced concrete structures; however, its labor-intensive nature greatly reduces automation efficiency.

With the above limitations identified, the authors previously proposed a bio-inspired solution, namely “knitting” and “tilting” printing strategies, to mitigate anisotropy [31]. This approach highlights two key features. First, ECC serves as a self-reinforcing printing ink, providing inherent tensile resistance and ductility. Second, the method eliminates the need for external reinforcement by relying solely on an innovative spatial toolpath design. Combined, these strategies maximize the design flexibility enabled by 3D printing technology while fully utilizing the superior mechanical properties of ECC. As a result, flexural strength in the vertical direction reached 5 MPa, representing an improvement of up to 179% compared to conventional parallel printing. Furthermore, cracks were observed originating from the designed interface system, along with notable crack deflection and bifurcation behavior. These findings validate the effectiveness of the proposed interface design. However, ductility enhancement in the weakest direction remained limited, making it challenging to achieve strain/flexural hardening behavior that is comparable to cast ECC.

To fill the research gap and further optimize the previously proposed printing patterns, this study introduces another innovative 3D printing strategy, namely “stitching”, aiming at mitigating anisotropy and enhancing ductility in the out-of-plane direction. Experimental validation was performed through four-point bending tests on printed ECC samples from three orthogonal orientations. The traditional parallel structure, as shown in Fig. 1, was printed and tested as a reference. Non-destructive techniques, including digital image correlation (DIC) analysis, acoustic emission tests (AET), and micro-CT scanning, were implemented to monitor damage progression and analyze failure mechanisms.

2. Architected strategy

Aligned with the philosophy of previous work [31], an architected printing strategy for 3DP-ECC was proposed and named “stitching”. This pattern encompasses four fundamental trajectories, including the combination of Straight/Wavy filaments (S/W) deposited along the orthogonal X/Y direction, as denoted in Fig. 2. The four basic elements are strategically layered in a specific sequence to achieve interweaving and interlocking of the filaments. Notably, “Wavy X” (WX) and “Wavy Y” (WY) incorporate a spatial structure involving the z-direction (out-of-plane direction), thereby transcending the constraints of conventional planar layer configurations.

This innovative three-dimensional design yields several benefits:

(1) Out-of-plane fiber alignment at the microscale. This strategy exploits the spontaneous fiber alignment along the printing direction observed in 3DP-ECC [4]. As the printing nozzle travels up and down, the fibers within the wavy filaments acquire a z-direction component, i.e., fibers are vertically inclined. This fiber orientation facilitates fiber bridging in the z-direction, generating out-of-plane tensile/flexural resistance. Previous study has demonstrated the effectiveness of this fiber allocation approach [31]. In contrast, traditional printing methods, characterized by planar filament configurations, usually lack cross-layer fibers [29], resulting in insufficient fiber bridging and leading to brittle or quasi-brittle behavior as interlayer cracks develop.

(2) Enhanced mechanical engagement at the macroscale. The wavy trajectories introduce interlocking features, such as grooves and teeth, which promote strong mechanical engagement between

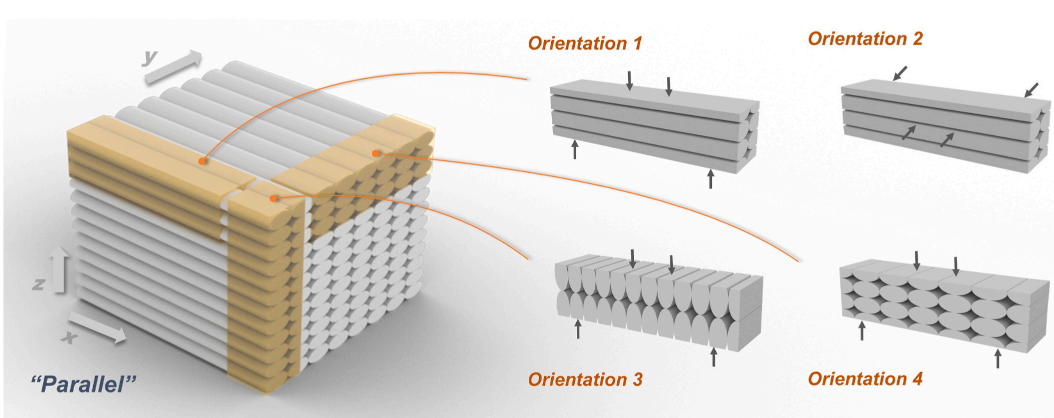

Fig. 1. Parallel printing and different loading orientations. The gaps between filaments are exaggerated to show their positions.

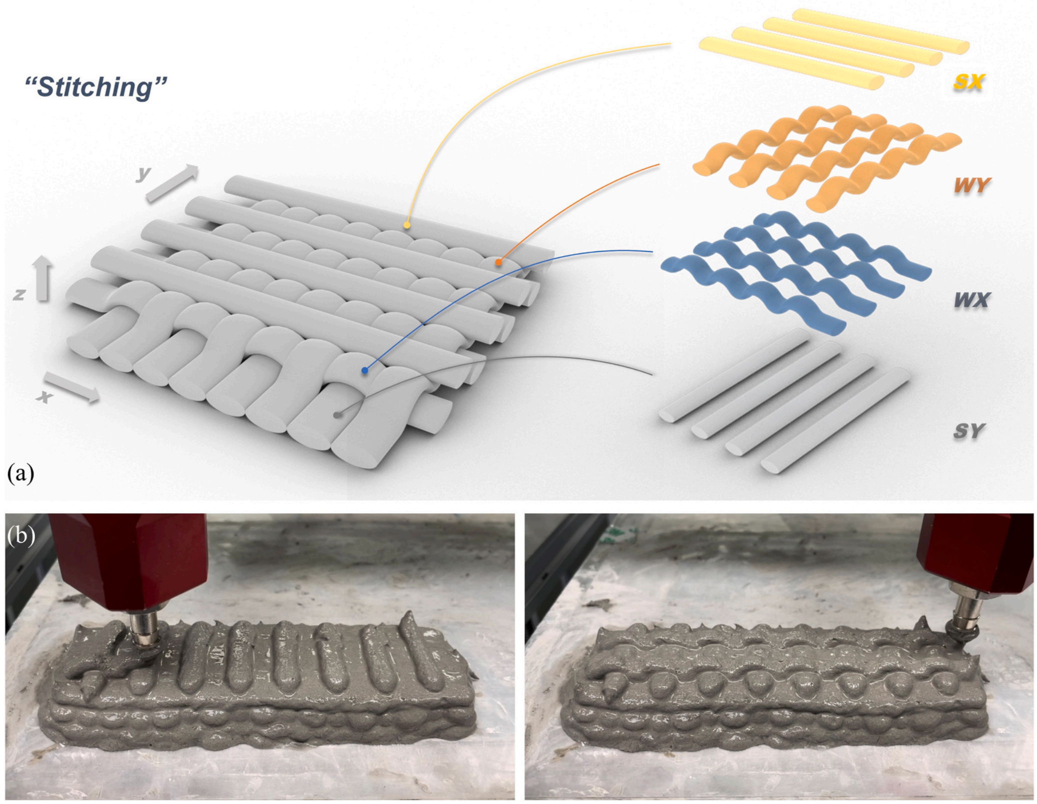

Fig. 2. (a) Schematic diagram of "stitching" pattern which possesses four fundamental trajectories, i.e., the combination of straight/wavy filaments (S/W) deposited along the X/Y direction. The gaps between filaments are exaggerated to show their positions. (b) Printing process of a miniaturized prototype.

layers. For instance, when "Wavy X" (WX) overlays "Straight Y" (SY), the grooves formed by adjacent SY filaments allow WX to fit in place, creating an interwoven structure. This interlocking effect maximizes interlayer bonding by exploiting the flexibility of 3D printing technology and promoting interactions between layers, strengthening the overall structure.

(3) *Increased interface complexity.* Beyond the notable mechanical interlocking, the braided structure also significantly enhances interface complexity, which plays a crucial role in energy dissipation during cracking and improves material toughness. This concept was inspired by biological structures found in nature, such as conch shells [65,66] and mantis shrimp [67,68], which achieve superior toughness through intricate three-dimensional microstructures (e.g., cross-lamellar or helicoidal arrangements) despite their brittle base materials. Similarly, the "stitching" pattern introduces complex interfaces that elevate fracture complexity, causing cracks to twist, deflect, branch and bifurcate rather than propagate linearly through unidirectional interfaces. These crack behaviors effectively dissipate fracture energy, leading to substantial improvements in ductility and toughness of the structure [69–71].

These features collectively counteract traditional issues associated with layer bonding and out-of-plane fracture behavior in 3D-printed concrete structures. By facilitating energy dissipation and increasing toughness, the "stitching" pattern addresses the long-standing anisotropy concerns, advancing the structural performance of 3D printed structures.

3. Experimental programs

3.1. Materials

The binders for printable ECC include blast furnace slag cement (CEM III/B, ENCI), silica fume (Elkem Microsilica®), and limestone powder (Calcitec®, Carmeuse), with a water-to-binder ratio of 0.26. The rheology of the fresh ECC was modified using superplasticizer Glenium 51. Micro polyethylene (PE) fibers (Dyneema®), 1.0 % dosage by volume, were employed for internal reinforcement. The mix proportions are provided in Table 1, while the fiber properties are summarized in Table 2.

During preparation, all dry ingredients were pre-mixed for 2 min, followed by the addition of water and superplasticizer, with mixing continued for another 4 min. The PE fibers were divided into four equal portions and added incrementally in separate batches, with a 2-min mixing interval between each addition. The printed ECC specimens were cured in an ambient room environment without any covering for 28 days.

The tensile properties of printable PE-ECC at 28 d are shown in Fig. 3. Cast dog-bone samples were uniaxially loaded at a fixed rate of 0.4 mm/min by a SCHENCK TREBEL machine. Two linear variable displacement transducers (LVDTs) measured the average tensile strain in the gauge region. The results indicated an average tensile strength of 4 MPa and a tensile strain capacity of approximately 2.0 %.

Table 1
Mix proportions of printable ECC (unit: kg/m^3).

Cement	Silica fume	Limestone	Water	Superplasticizer	PE Fiber
807	115	448	359	2.8	9.4

Table 2
Properties of micro PE fibers (provided by the manufacturer).

Length (mm)	Diameter (μm)	Solid density (g/cm^3)	Tensile strength at break (GPa)	Tensile modulus (GPa)	Elongation at break (%)
6	40	0.97–0.98	3.0	110	2–3

3.2. Printing setup

The lab-scale 3D printing setup in TU Delft is illustrated in Fig. 4. Freshly mixed material was first fed into the hopper of a progressive cavity pump (PFT Swing M). A pressure gauge was installed at the rotor-stator outlet of the pump to monitor pressure fluctuations. The material was extruded through a PFT hose and a circular down-flow nozzle with a diameter of 20 mm. Both the nozzle and the hose end were mounted on the beam of a 3D freedom Computer Numerical Control (CNC) machine, which controlled the movement and positioning of the extrusion system according to a predefined G-code. The nozzle's traveling speed was adjusted according to path geometry to account for the printer's inherent system response time. To maintain consistent printing quality, a programmed velocity of 8 m/min was used for wavy filament deposition, while a lower velocity of 5 m/min was applied for straight filament printing. The layer thickness of all printed structures in this study

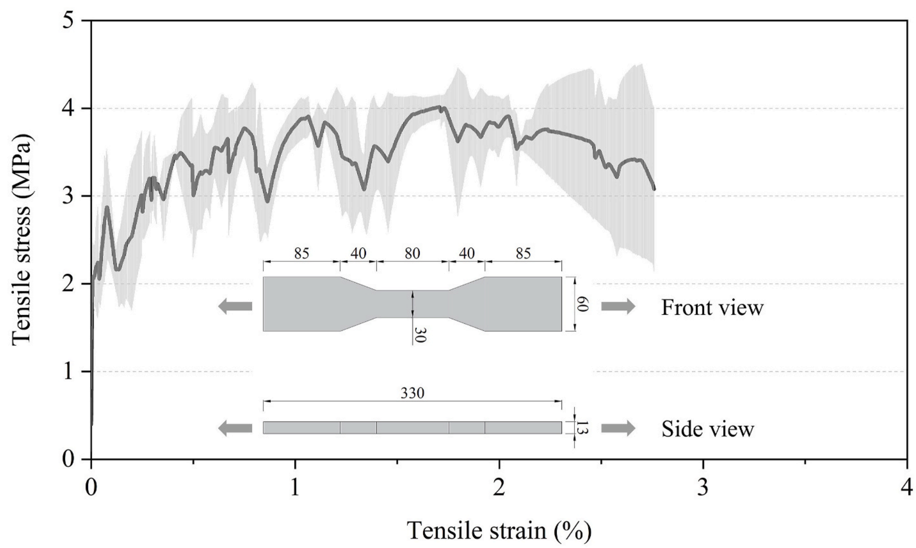

Fig. 3. Tensile properties of printable PE-ECC and dog-bone sample geometries. The solid line shows an average of three samples, while the shaded area represents the standard deviation.

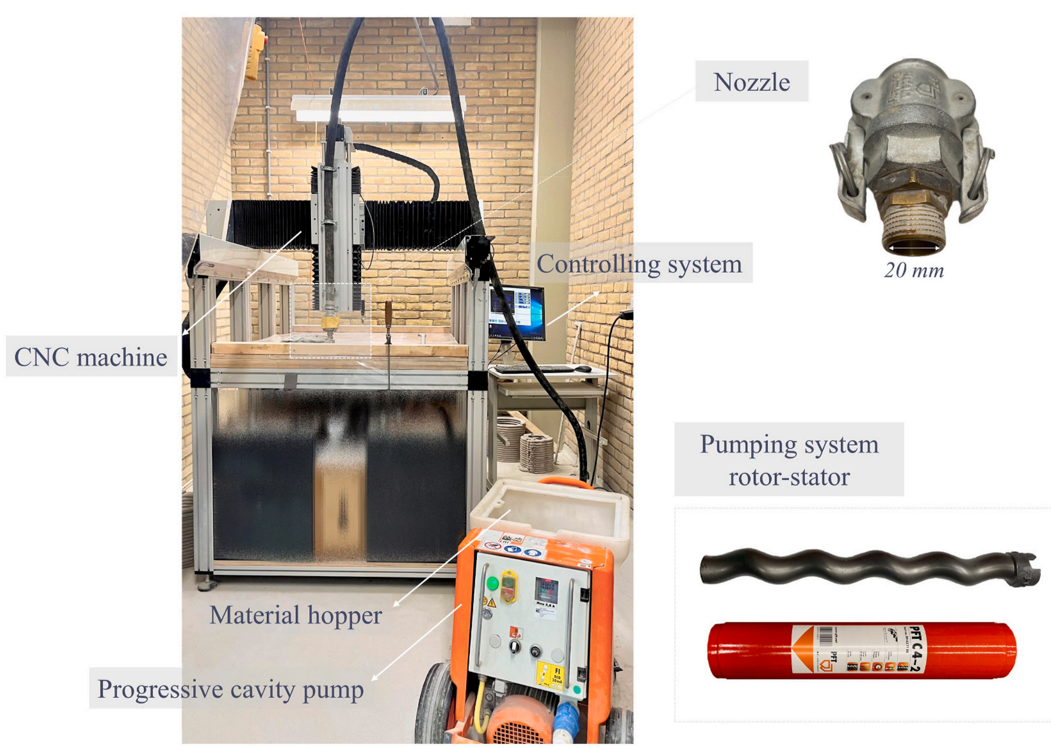

Fig. 4. Printing setup.

was maintained at 12 mm. The center-to-center distance between two adjacent filaments was set at 30 mm.

3.3. Test setups

The ECC specimens for bending tests were saw-cut from printed structures along two directions, the x-direction and the z-direction, with dimensions of 40 mm × 40 mm × 160 mm. These samples were then loaded in three different orientations, i.e., Orientation 1, 2, and 3 shown in Fig. 1. It is worth noting that Orientation 4 is identical to Orientation 1 for the stitching pattern, as this pattern presents the same filament arrangement along the x- and y-directions.

The setups for the four-point bending tests consisted of three main components (Fig. 5): (1) the loading setup, (2) the acoustic emission test (AET) system, and (3) the digital image correlation (DIC) system. The tests were performed on an Instron 8872 machine, with loading and supporting spans of 40 mm and 110 mm, respectively. The machine loading rate was maintained at 0.3 mm/min. One LVDT was attached to the loading plate to record the vertical displacement.

Two acoustic sensors (Wideband Differential (WD) AE sensors with an operating frequency range of 100–900 kHz) were attached to the front surfaces of the ECC specimens to capture acoustic signals generated by sample damage. The sensors were secured using elastic rubber bands, with high vacuum grease applied between the sensor surface and the specimen. Acoustic data were recorded by a Micro-II Express AE Chassis (Mistras Group, Inc) and analyzed with MATLAB.

For DIC analysis, random black speckles were sprayed onto the front surface of the ECC specimens over a base coat of white paint. A high-resolution camera was used to record the surface deformation of the samples during loading. The images were then analyzed using GOM Correlate software.

Post-failure ECC specimens were subjected to helical scanning along the longitudinal axis with a voxel thickness of 50 μm, using a TESCAN CoreTOM micro-CT scanner. The sequentially acquired slices were stored as 16-bit image files, then reconstructed using StudioMax software and visualized in Dragonfly software to elucidate the internal crack pattern.

4. Results and discussion

4.1. Flexural performance

The test results of four-point bending are summarized in Fig. 6. For printed ECC, different loading scenarios are denoted using the printing pattern abbreviation (“PA” for “parallel”, “ST” for “stitching”) combined with the loading orientation (1/2/3). For instance, ST2 represents stitching specimens loaded in Orientation 2.

Parallel-pattern specimens outperformed their cast counterparts in both Orientations 1 and 2, as illustrated in Figs. 6(a) and 7. Among all groups, PA1 exhibited the highest flexural strength and energy dissipation capacity, with average values reaching 136 % and 192 % of the cast ECC, respectively. PA2, while slightly inferior to PA1, also demonstrated enhanced performance. This exceptional bending behavior in these two orientations can be attributed to two primary factors:

(1) *Fiber alignment.* The tendency of fibers to align with the direction of shear flow during extrusion has been well-documented in previous studies [23,31]. The fiber alignment along the nozzle traveling path maximizes crack-bridging capability in this orientation, significantly enhancing the tensile and flexural performance relative to cast counterparts with randomly oriented fibers. In parallel printing, fibers tend to align along the x-direction, which coincides with the crack opening direction for PA1 and PA2. As a result, the fiber-bridging effect is particularly efficient in these two directions, contributing to superior overall performance compared to cast ECC.

(2) *Crack-trapping effect.* In laminate structures, various interfacial crack modes can be observed. In perfectly brittle materials, interfacial cracks tend to propagate straight through the interface, as the crack growth resistance remains constant along the interface [72], as illustrated in Fig. 8(b). However, in real-world materials, crack deflection and kinking are commonly observed in laminate structures. As an interfacial crack progresses along the interface, it can deflect into the bulk material of the adjacent layer. If the bulk material is quasi-brittle, the kinked crack

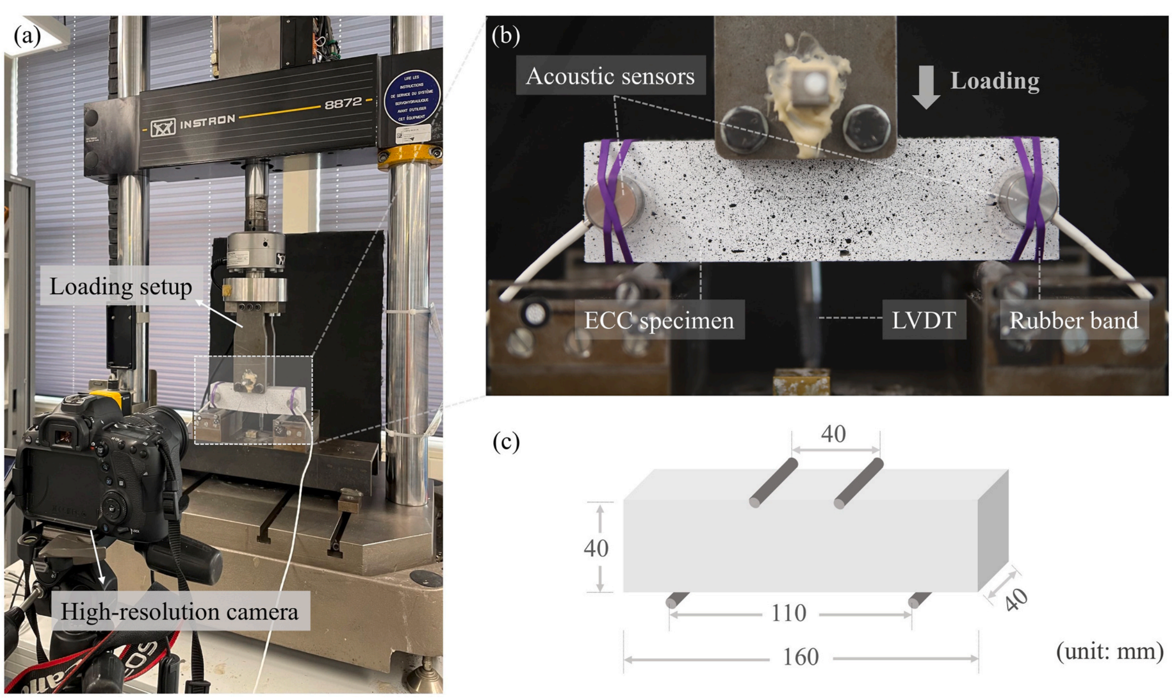

Fig. 5. Test setups for four-point bending tests.

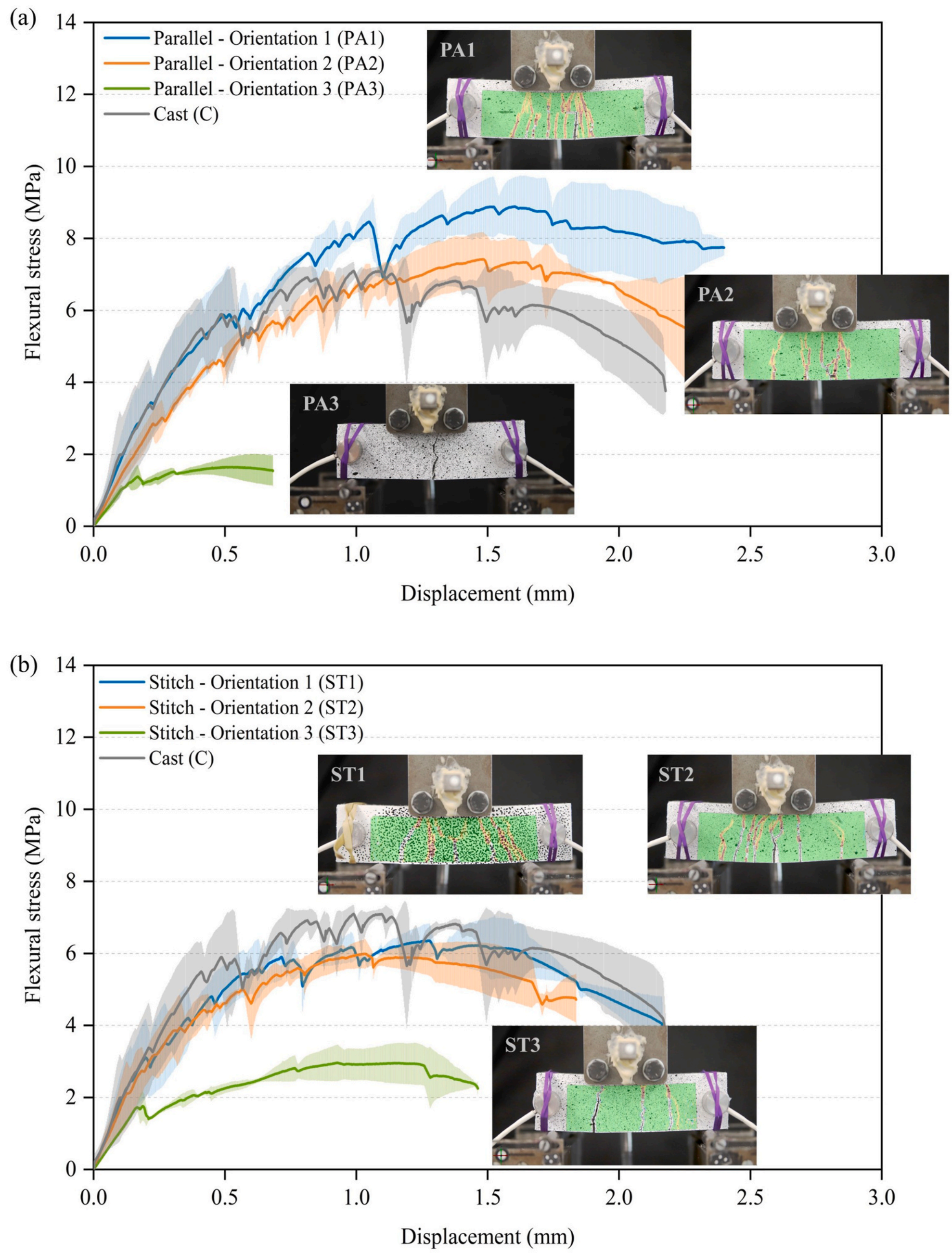

Fig. 6. Flexural properties of printed ECC and cast reference. Each solid line curve represents an average of three tested samples in a group, while the shaded area shows the standard deviation. The red and yellow regions in DIC images indicate crack openings (ε_{xx}, strain in the horizontal direction) at peak stress. (For interpretation of the references to colour in this figure legend, the reader is referred to the Web version of this article.)

typically penetrates the layer and reorients back into the next interlayer interface [73,74]. This fracture behavior facilitates energy dissipation and serves as an effective strategy to enhance the toughness of quasi-brittle materials through architected structures [69]. In ductile materials like ECC, however, an additional crack-trapping effect is evident. When the interfacial crack tip progresses into the bulk layer, the presence of fibers significantly enhances crack growth resistance or fracture toughness. This rapid rise in the R-curve (Fig. 8(b)) effectively restricts further crack propagation (Δa), as increasing amounts of energy must be dissipated through plastic deformation for the crack to continue to grow [73,75]. The combined kinking-trapping effect repeatedly deflects the interfacial crack into the bulk layer, only to be halted by the fibers, thereby dissipating substantial energy and increasing material toughness.

The synergistic action of the above factors contributed to the remarkable flexural performance of PA1 and PA2. Dense multiple cracking, indicative of ductile behavior, can be observed in the DIC analysis images in Fig. 6(a). Horizontal interfacial cracks and kinked vertical cracks were observed in PA1 specimens, with a close-up image shown in Fig. 8(a).

However, PA3 presented a sharp contrast to the preceding two orientations. In the four-point bending test, a localized crack was observed with minimal crack deflection. A single dominant crack propagated through the specimen, corresponding to significantly lower strength and toughness compared to the other groups. The average flexural strength

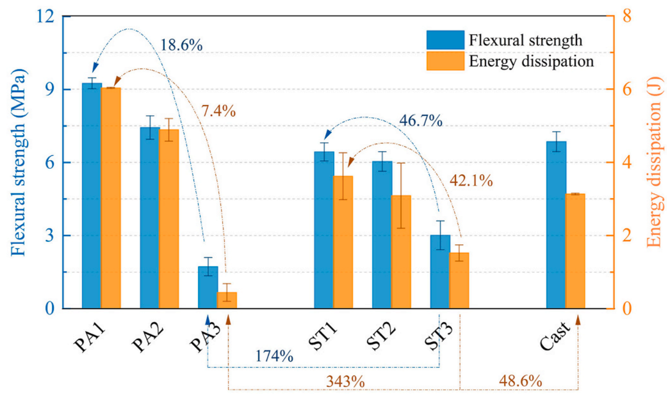

Fig. 7. Flexural strength and energy dissipation of printed and cast ECC. Energy dissipation is calculated from the onset of loading to the peak load, excluding the softening phase.

of PA3 amounted to 18.6 % and 28.2 % of that of PA1 and cast ECC, respectively. Moreover, the energy dissipation of PA3 was merely 7.4 % of PA1 and 14.0 % of cast ECC. A transient increase in flexural stress after crack initiation indicated the presence of cross-layer fiber bridging; however, the resistance of limited fibers was quickly exhausted before failure. In this case, the ductility of the printed structure in the out-of-plane direction was severely undermined, exhibiting pronounced anisotropy.

For the stitching pattern, the performance of ST1 and ST2 was comparable to the cast reference (see Figs. 6(b) and 7). DIC analysis images revealed that both ST1 and ST2 exhibited extensive multi-cracking, along with notable crack branching and bifurcation. The propagation of cracks is governed by their tendency to advance along structural weak points—regions with the least resistance to driving force ratio, such as interfaces—indicating that the interface system's morphology can directly impact the trajectory and behavior of cracks. In contrast to the unidirectional, parallel planar interfaces created by parallel printing, the stitching pattern forms a more intricate system with multidirectional, interwoven interfaces in a three-dimensional space, rendered by the complex filament orientations. Consequently, the spatial configuration of the interfaces induces significant crack deflection and bifurcation in stitched ECC. This is most evident in ST1, where the central vertical crack was bifurcated into a "Y" shape, influenced by the orthogonal filament pointing in/out of the paper. The characteristics of this interface system will be further elaborated in the next sub-section through micro-CT scan results.

In the weakest Orientation 3, the stitching pattern exhibited impressive performance enhancement. Fig. 6(b) highlights the remarkable flexural hardening behavior of ST3. Accompanied by the development of 3 to 4 primary cracks with internal deflections (as will be demonstrated in the CT results subsection), the flexural stress of ST3 continued to rise, with several minor load drops. The flexural strength was promoted to 174 % of PA3 in the same loading direction, while the energy dissipation reached an extraordinary 343 %. The energy dissipation capacity, which is directly related to material toughness, was also measured at 48.6 % of cast ECC, confirming its exceptional ductility. A comparison of anisotropy indices also revealed that ST3 achieved 46.7 % of the strength and 42.1 % of the energy dissipation of ST1, highlighting the substantial anisotropy mitigation of ST compared to PA printing strategy.

It is worth noting that, however, the trade-off between the performance in Orientations 1/2 and in Orientation 3 is almost inevitable. The parallel pattern maximizes the fiber alignment along the x-direction, while "stitching" redirects some of the fibers to the y- and z-directions, thereby "diluting" the fibers' reinforcing ability in the x-direction. Therefore, the performance reduction of ST1/ST2 relative to PA1/PA2 is anticipated. This trade-off partially contributes to the improvement in anisotropy metrics, e.g., the ST3-to-ST1 strength or energy ratio compared to the PA3-to-PA1 ratio, as the denominator decreased. However, it is important to emphasize that the absolute enhancement in ST3's properties is substantial, and its flexural hardening behavior represents a fundamental improvement compared to the quasi-brittle behavior of PA3.

The enhanced ductility of ST3 highlights the effectiveness of the "stitching" strategy in mitigating anisotropy. To the best of the authors' knowledge, no previous studies have reported strain- or flexural-hardening behavior in the out-of-plane direction for 3D-printed structures without external reinforcement. Given that structural integrity and resilience necessitate ductile behavior to prevent brittle failure, the architected strategy introduced in this study represents a pioneering and highly valuable advancement in automated concrete construction.

4.2. Micro-CT image analysis

To gain deeper insights into the interface distribution and failure mechanisms inside 3DP-ECC, damaged specimens in four-point bending were scanned using micro-CT. The bent specimens underwent helical scanning, and the mid-span sections—encompassing all cracked regions—were selected for visualization. For PA1 and ST1 (Figs. 9 and 10), the volumes analyzed spanned approximately 40 mm × 40 mm × 110 mm (representing the region between supporting spans), while the volumes of interest for PA3 and ST3 (Figs. 11 and 12) were approximately 40 mm × 40 mm × 90 mm in the middle section of the specimen.

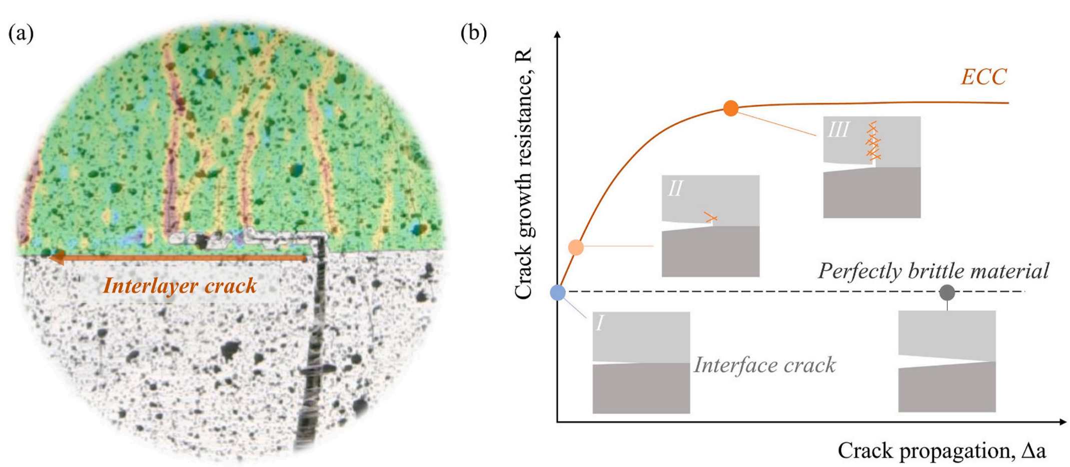

Fig. 8. (a) Crack kinking-trapping in printed ECC, and (b) schematic diagram of R-curve.

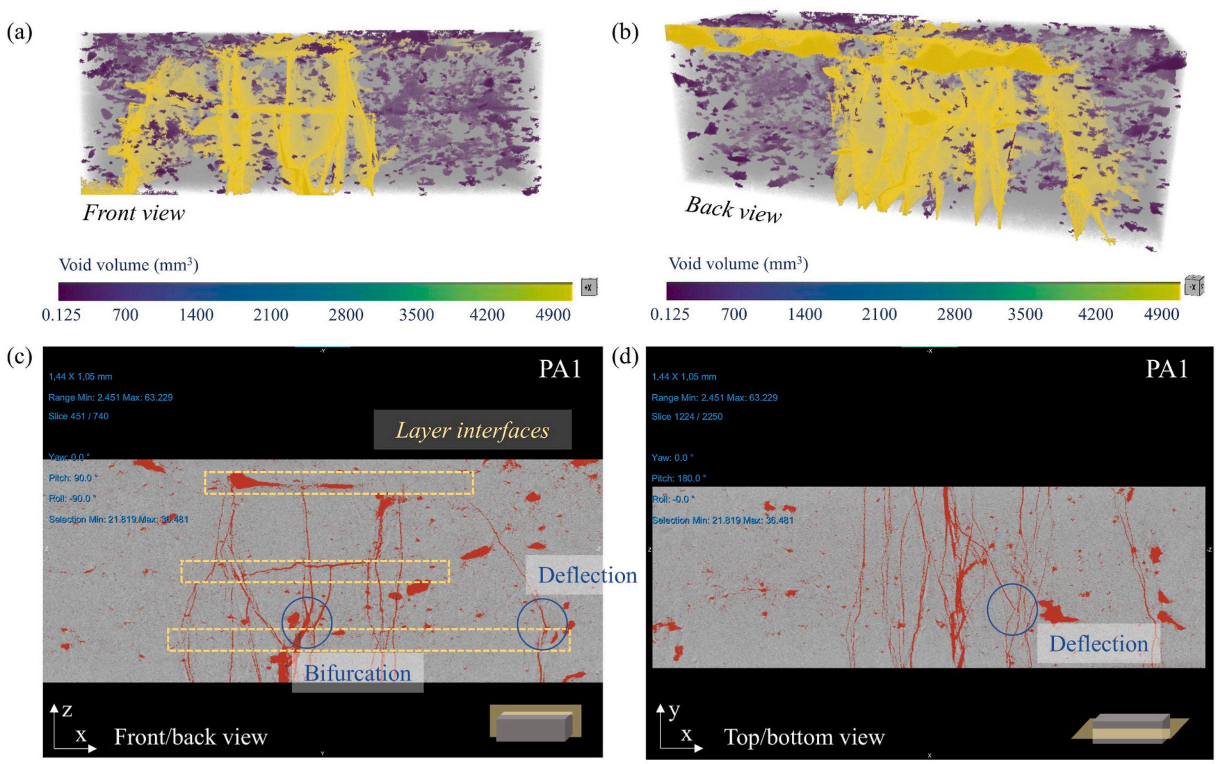

Fig. 9. Reconstructed micro-CT images of PA1 sample: (a–b) 3D rendered image and (c–d) cross-sectional slices, where red regions represent cracks and voids. (For interpretation of the references to colour in this figure legend, the reader is referred to the Web version of this article.)

Fig. 9 illustrates the reconstructed micro-CT images of PA1, showing the positions of three parallel interlayer interfaces. While horizontal cracks were absent at the lowest interface, significant deflection and bifurcation cracks occurred upon reaching the region indicated by the dashed box in Fig. 9(c). The second interface emerged as a critical location connecting the entire crack network. Cracks initiated in the lower layer propagated horizontally along this interface, bridging several vertical cracks before kinking upward into the upper layer. The presence of multiple layer interfaces in the buildup direction (z-direction) facilitated substantial crack deflection in PA1. In the x-y plane, the cracks exhibit a pronounced parallel alignment, with inter-filament interfaces causing only minor deflections, as shown in Fig. 9(d).

The cracking behavior of ST1 highlights the intentional engineering of 3DP-ECC's structure by architected paths, which facilitates filament interactions in both in-plane and out-of-plane directions. Fig. 10(a) and (c) depict how the mid-span crack bifurcated into a "Y" shape within the x-z plane. The vertical crack first encountered a curved interface (Fig. 10 (d)) and propagated along it, then underwent kinking and trapping as it traversed the interface. The curvature of the interface arose from the interweaving of orthogonal filaments within the x-y horizontal plane, such as the wavy interface generated when WY passed above and below SX. Similar crack-interface interactions were also observed in the x-y plane— bifurcation took place when a crack advanced to a filament intersection, encountering the contour of a wavy filament (Fig. 10(e)).

These findings substantiate the effectiveness of the engineered interface system in modulating crack propagation. The "stitching" pattern deliberately obscures the distinction between inter-layer and inter-filament interfaces through strategic design, as filaments interact across multiple planes. This intricate interface system precipitates frequent changes in crack trajectories, thereby inducing the desired structural responses.

The internal crack morphology of PA3 aligned with the observed surface crack pattern. A localized crack extended through the full sample height with minor deflection (Fig. 11(a)). It propagated predominantly in the vertical direction, resulting in rapid penetration.

In contrast, ST3 exhibited a markedly different crack pattern. Fig. 12 (a) and (b) illustrate multiple primary cracks, with the right crack showing pronounced twisting. On the x-z plane slice (Fig. 12(c)), cracks demonstrated a zigzag trajectory during upward propagation, repeatedly altering the intrusion direction of the crack tip. The far-right crack exemplified a typical pattern: initially, the crack deviated laterally from the vertical axis, inclining to the right before realigning with its original direction; subsequently, during the formation of the "crack tree", the crack underwent frequent large-angle deflections and bifurcations. However, these branches were swiftly arrested and stopped by fibers, confirming that fiber orientation has been diversified by the printing path, enabling effective crack capture and bridging from multiple directions. Similarly, on the x-y plane (Fig. 12(d)), jagged-shaped cracks and pronounced deflections were also evident. This consistency in crack behavior across different planes highlights the similar fracture patterns in the inter-filament and inter-layer directions, indicating a mitigation in anisotropy.

In this study, micro-CT scanning plays a critical role in unveiling the internal crack morphology, revealing key characteristics and phenomena that could not be effectively captured through surface observation techniques, for example, the frequent transitions in crack behavior inside the structures. Through the micro-CT analysis in this sub-section, the hypotheses presented in Section 2 regarding the interface system and its influence on crack patterns are validated, offering valuable insights into the effectiveness of the proposed strategy.

4.3. *Acoustic emission analysis*

Acoustic emission (AE) tests were conducted simultaneously with four-point bending tests to monitor damage progression. Each AE event represents an isolated and distinct occurrence, e.g., crack initiation and propagation, fiber debonding, sliding, breakage, etc. Only signals exceeding a predefined threshold are recorded. These signals are

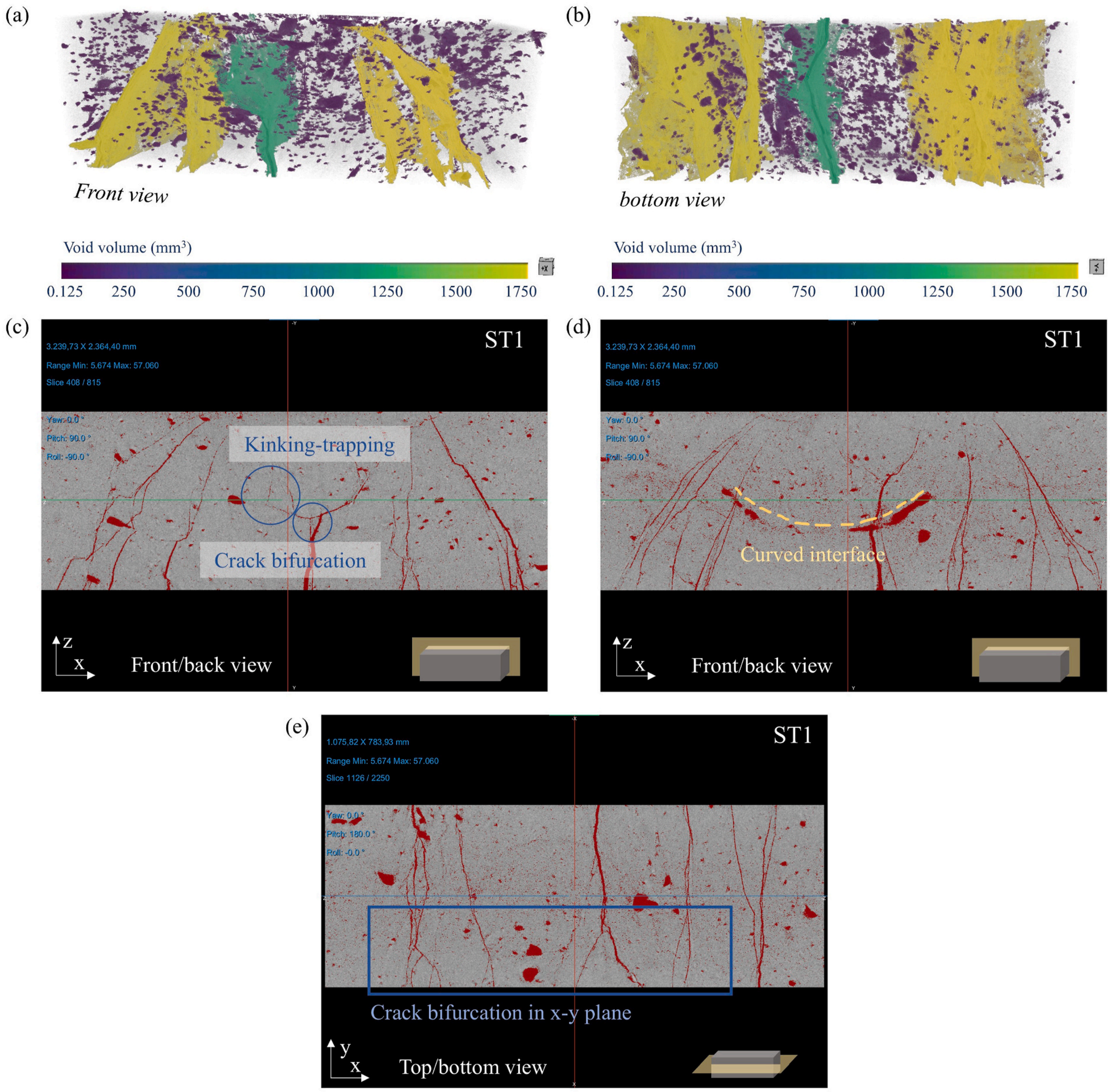

Fig. 10. Reconstructed micro-CT images of ST1 sample: (a–b) 3D rendered image and (c–d) cross-sectional slices, where red regions represent cracks and voids. (For interpretation of the references to colour in this figure legend, the reader is referred to the Web version of this article.)

characterized and differentiated based on various parameters [76,77], including rise time, peak amplitude, signal count, and signal duration. It should be noted that the AET analysis presented in this paper was conducted using data from a single sensor, as the two sensors were asymmetrically positioned and collected a highly consistent volume of signals with minimal deviation.

Fig. 13 illustrates the development of accumulated acoustic emission (AAE) events and AE event rate for printed ECC. AAE represents the cumulative number of AE signals, while AE event rate quantifies the number of events detected per unit time. By examining these parameters alongside the load-time curve, three typical phases of the mechanical response can be identified during the damage evolution: (I) *Microcrack Initiation*, (II) *Crack Propagation*, and (III) *Accelerated Damage*.

Phase I corresponds to the elastic region leading up to the first crack initiation. During this phase, the AAE curves exhibit a gradual and steady increase, with minimal accumulation, as microcracking is the dominant mechanism. The initial burst of AE events typically coincides with the onset of the first crack.

Phase II represents the crack propagation phase, encompassing both matrix cracking and fiber pullout or breakage. Mechanically, this phase corresponds to the flexural-hardening plateau. The flexural hardening behavior, driven by the steady cracking mechanics of ECC, is marked by small load drops associated with multiple crack formations. These load drops are accompanied by spikes in the AE event rate and step-like increments in AAE, which are most pronounced in PA1 and ST1 due to their more notable flexural-hardening responses.

Phase III typically corresponds to the post-peak softening stage. During this phase, the AAE curve stabilizes or exhibits a slight reduction in slope (as in Fig. 13(d)), while the AE event rate is marked by consistent minor bursts. At this stage, the formation of new cracks is limited; instead, the structural response is dominated by the opening and widening of main cracks and the pullout or fracture of fibers. Although the accumulation of AE signals does not increase significantly, this phase is characterized by accelerated structural degradation and onset of ultimate failure.

To differentiate fracture phenomena, AF (Average Frequency)-RA analysis was conducted to classify damage types [78–81]. AF is defined as the ratio of threshold crossing counts to signal duration, with

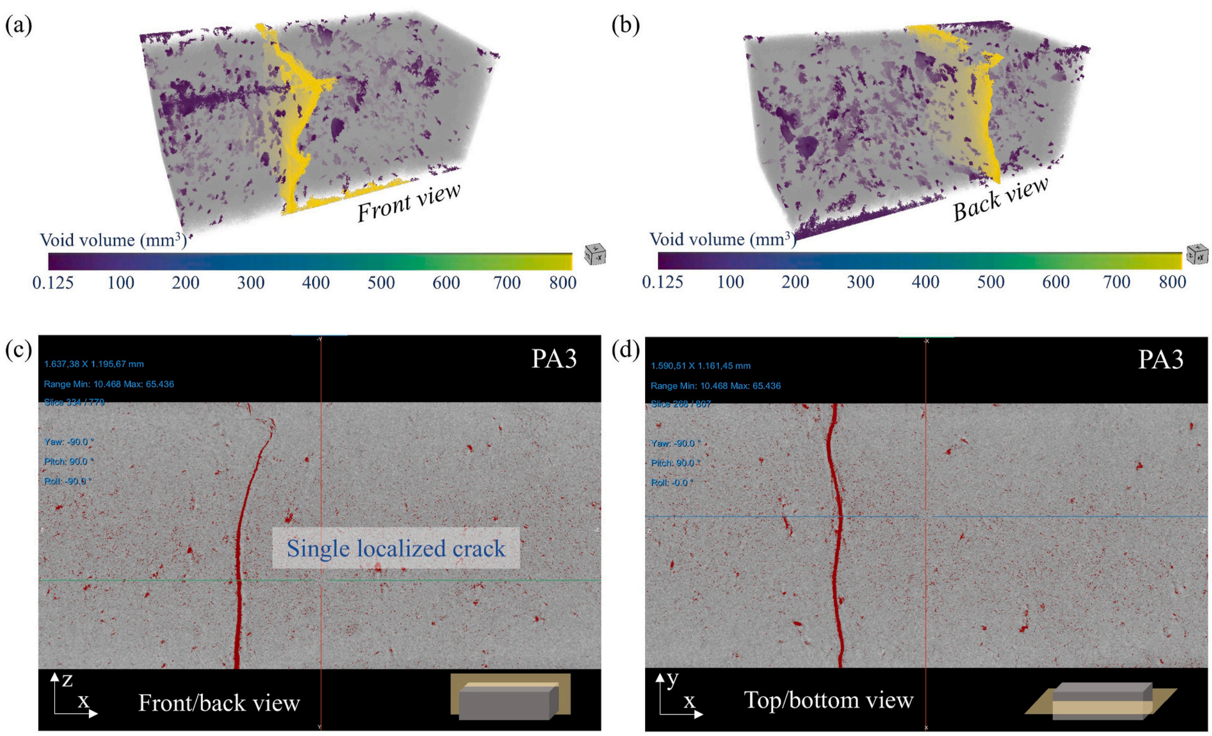

Fig. 11. Reconstructed micro-CT images of PA3 sample: (a–b) 3D rendered image and (c–d) cross-sectional slices, where red regions represent cracks and voids. (For interpretation of the references to colour in this figure legend, the reader is referred to the Web version of this article.)

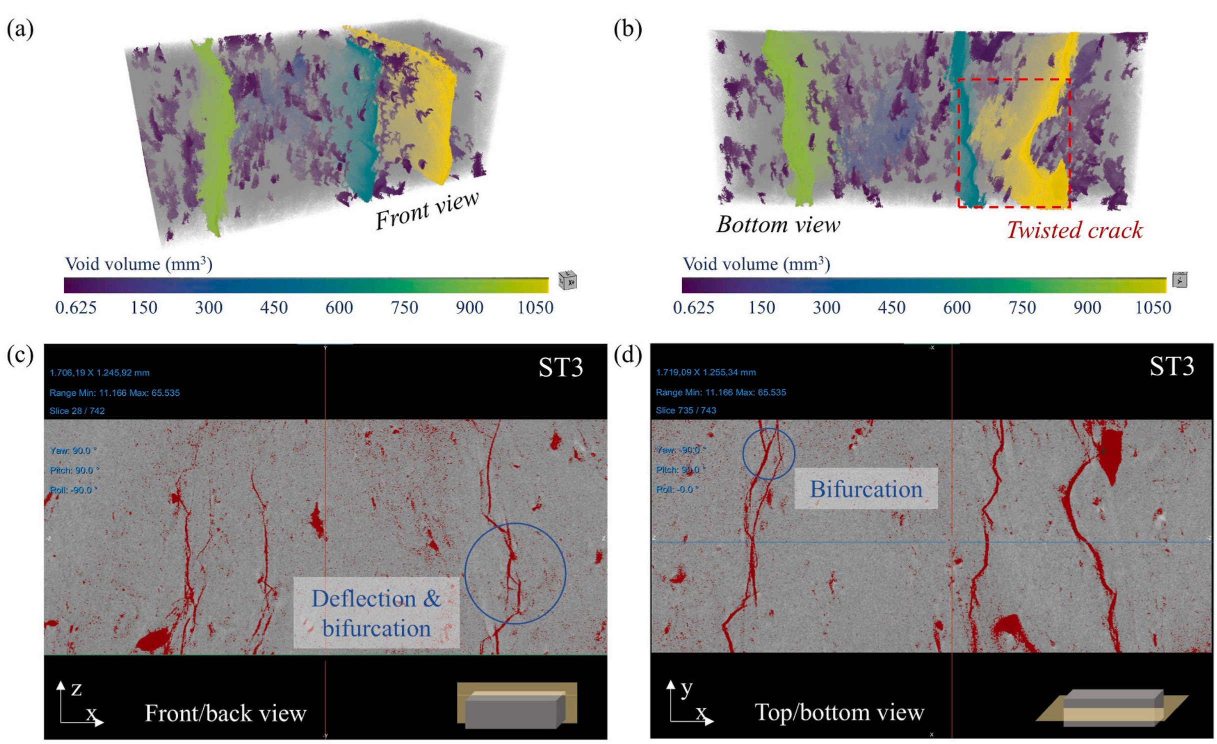

Fig. 12. Reconstructed micro-CT images of ST3 sample: (a–b) 3D rendered image and (c–d) cross-sectional slices, where red regions represent cracks and voids. (For interpretation of the references to colour in this figure legend, the reader is referred to the Web version of this article.)

high AF values reflecting sharp, high-frequency signals. RA represents the ratio of rise time to peak amplitude, therefore higher RA values suggest slower crack propagation. By analyzing AF and RA, crack types can be classified: high AF and low RA typically indicate tensile cracks (Mode I), while low AF and high RA are associated with shear cracks (Mode II), commonly linked to interfacial debonding or frictional sliding.

As shown in Fig. 14, AF-RA scatter plots illustrate individual AE signals grouped according to occurrence time. As loading progressed, the data clusters migrated from the upper-left to the lower-right,

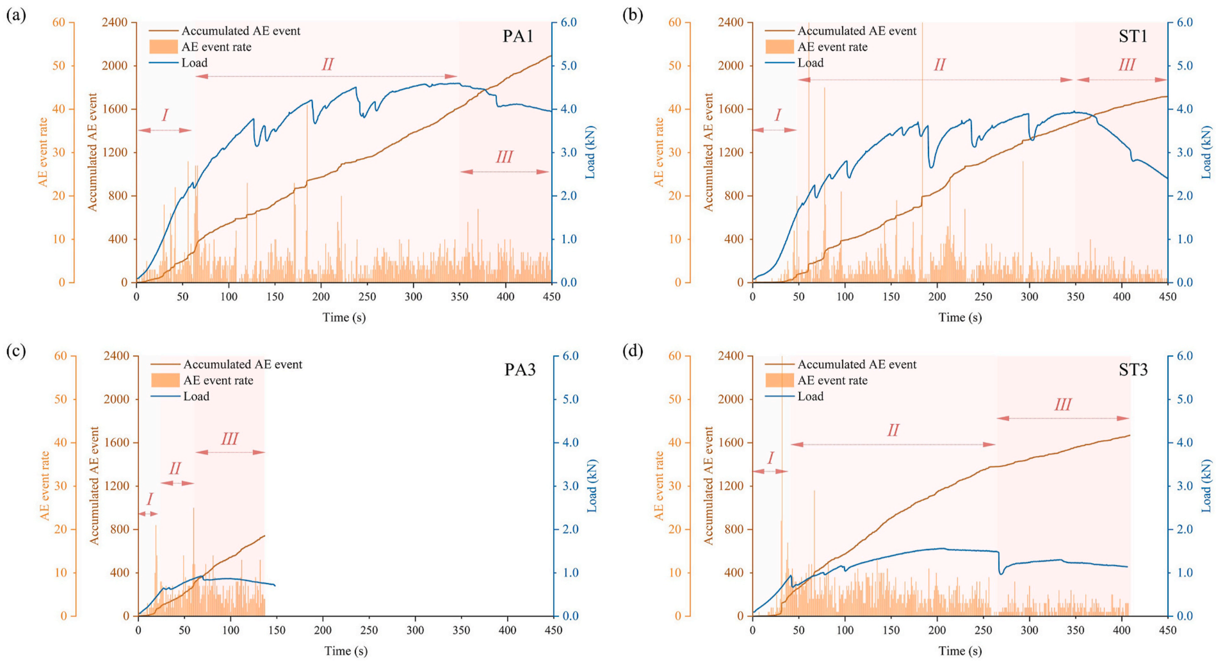

Fig. 13. Accumulated AE event and AE event rate for printed ECC under four-point bending.

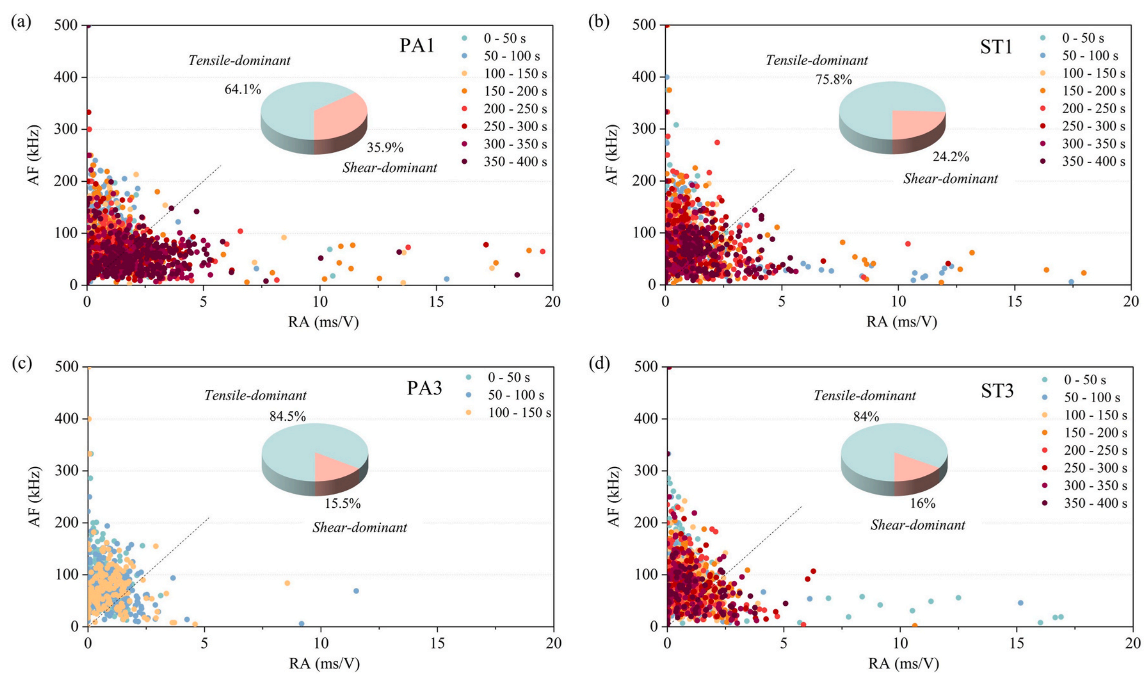

Fig. 14. Correlation between RA and AF. Pie charts show the signal count proportion above and below the dividing line, which signifies crack classification.

indicating a transition in the dominant failure mode. Early-stage failure features high-frequency, sharp tensile cracks (upper-left), while later stages contain more slow, sustained shear failure and frictional sliding (lower-right).

To establish a crack classification threshold, AE signals recorded before the initial crack in each group were plotted together. A dividing line was fitted such that 90 % of signals fell above it, representing tensile-dominant cracks, while signals below the line indicated shear-related cracks, as illustrated in Fig. 15. This universal dividing line (plotted as dashed lines in Fig. 14) was applied to all 3DP-ECC groups, and the proportion of signals on each side was quantified and illustrated using pie charts.

Crack classification provides valuable insights into the microscopic damage mechanisms. With comparable numbers of recorded signals, PA1 demonstrates a higher proportion of shear-dominant cracks than ST1 (see Fig. 14(a) and (b)). This suggests that PA1's failure process was governed by mechanisms such as fiber-matrix debonding, fiber pull-out, and shear sliding, highlighting the critical role of fiber bridging in stabilizing crack propagation and delaying catastrophic failure. Conversely, ST1's damage evolution is more reliant on Mode I crack openings characterized by tensile-driven fractures. This observation aligns with experimental findings and supports the intended function of the stitching strategy, that is, promoting crack initiation and deflection to enhance ductility. Furthermore, the reduced presence of shear-

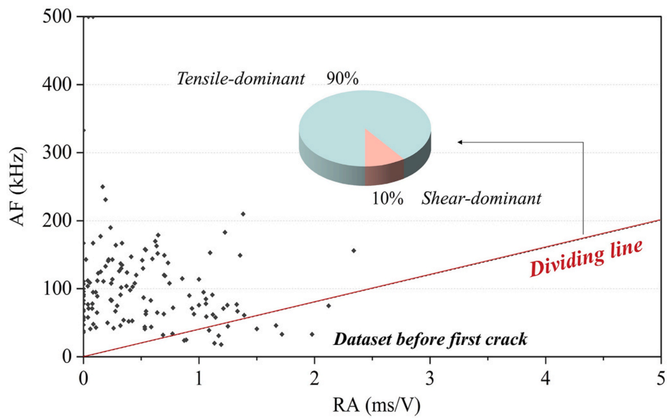

Fig. 15. Determination of the dividing line.

dominant cracks, commonly linked to fiber debonding and pull-out, indicates that the intentional diversification of fiber orientations inevitably impaired fiber bridging efficiency along Orientation 1.

The total number of AE signals recorded for ST3 is more than double that of PA3, as indicated by the accumulated AE events in Fig. 13, signifying a markedly higher occurrence of both tensile- and shear-dominant cracks in ST3. Therefore, despite the similar proportion in pie charts (see Fig. 14(c) and (d)), the absolute number of both types of fracture signals in ST3 exceeds that of PA3 by more than twofold. This highlights ST3's enhanced crack-opening and fiber-bridging capacities compared to PA3.

In comparison to Orientation 1 (PA1 & ST1), the proportion of shear-dominant cracks in Orientation 3 specimens (PA3 & ST3) is notably lower. This reduction originates from the fact that, in the out-of-plane direction, the mechanical behavior of 3DP-ECC is primarily governed by the development of tensile cracks and a relative lack of fiber bridging. This observation leads to two key inferences:(1) Although ST3 demonstrates an improved fiber-bridging capacity relative to PA3, the number of fibers available for out-of-plane reinforcement remains considerably lower than that in ST1; (2) cracking induced by the engineered interface complexity serves as the primary contributor to the enhanced ductility of ST3.

In summary, AET analysis reveals that the "stitching" strategy substantially increases the overall proportion of Mode I fracture, characterized by tensile-driven crack opening. This aligns with the anticipated failure mechanism, wherein ductility enhancement is primarily achieved through controlled fracture. Additionally, improvements in the fiber-bridging capacity of ST3 are evident, verifying assumptions about fiber orientation distribution in the design philosophy. However, the primary driver of its superior performance remains the intentional design of crack propagation enabled by the engineered interface architecture.

5. Core strengths, application prospects and challenge

The proposed printing strategy - "stitching" -represents a significant advancement over the authors' previous work. While building upon the same theoretical foundation, "stitching" demonstrates superior advantages and broader potentials compared to the previously introduced "knitting" and "tilting" patterns:

(1) *Enhanced performance.* Compared to previous printing strategies which focused solely on promoting strength, "stitching" delivers a marked improvement in ductility by exhibiting flexural-strengthening behavior in the out-of-plane direction. This weakest direction of 3D-printed structures is notably strengthened, reaching approximately half the mechanical properties of conventional cast ECC— representing a substantial breakthrough. Such enhancement is critical for improving the overall structural integrity and resilience of 3D-printed components.

(2) *Tunable and customizable design.* The performance of the "stitching" pattern can be tailored and tuned through deliberate parameter design, offering potential opportunities for structural performance customization. Several variables within the "stitching" configuration allow for enhanced design flexibility. For instance, while the X and Y directions of the basic trajectory are orthogonal in the current study, the angle between them can be modified to alter in-plane mechanical properties and influence the morphology of the interface system (Fig. 16(a)). The stacking sequence of the four basic elements, currently arranged in the order "SX-WY-WX-SY" (top to bottom), can be adjusted to enable alternative configurations such as "SX-WY-WX-WX-SY" or "SX-WY-WY-WX-SY" (Fig. 16(b)). Such adjustment could modify the vertical amplitude of wavy filaments, impacting the mechanical interlocking and fiber distribution and thereby influencing the out-of-plane performance. Moreover, combining the "stitching" approach with the previously established "tilting" strategy [31] (see Fig. 16(c)), which involves printing structures at an overall tilt angle, presents another promising direction for improving out-of-plane strength.

(3) *Broader application scenarios.* Previous printing strategies are relatively rigid in accommodating complex geometries, as they require thick, block-like structures. In contrast, the "stitching" strategy enables greater geometric flexibility. Since the fundamental functional unit consists of a thin "composite layer" (formed by four basic elements and equivalent to twice the filament thickness), the overall structure can be designed with varying thicknesses and curvatures, resembling a flexible, fabric-like material. This adaptability greatly enhances the practical value of the proposed printing strategy, particularly in applications requiring structural components with complex loading conditions and geometric freedom. Potential applications include shells, domes, slabs, and other architectural or engineering elements where enhanced out-of-plane performance is critical. It is worth noting that, for such complex components, the incorporation of external reinforcement, such as custom-fabricated steel bars or meshes with specialized curvatures and geometries, typically involves considerable labor and cost. In that case, a printing strategy that gains reinforcement from material-intrinsic properties and architected structures offers a more efficient and economical solution.

In addition to the advantages and prospects discussed above, the limitation and potential improvement of the current printing strategy should be noted. This study employed a downflow nozzle, which introduces a collision risk between the nozzle and previously printed material in the downstream segment of wavy filaments. To avoid geometric deviations or excessive cavities caused by this issue, the geometry of the downward segment was adjusted to reserve additional space for the nozzle's movement, resulting in an asymmetrical trajectory compared to the upstream segment. While this adjustment has a negligible impact on printing efficiency and time, it adds complexity to path programming. This limitation stems primarily from the constraints of the gantry printing device, and therefore could be avoided by utilizing a six-axis printer/robotic arm with greater degrees of freedom. Such a system would allow the nozzle to rotate in space and maintain alignment with the printing path's tangent direction, eliminating the collision risks.

6. Conclusions

The present study proposed and validated a pioneering architected printing strategy – "stitching" – for 3D printing of ECC. The proposed strategy effectively promoted structural integrity by enhancing the out-

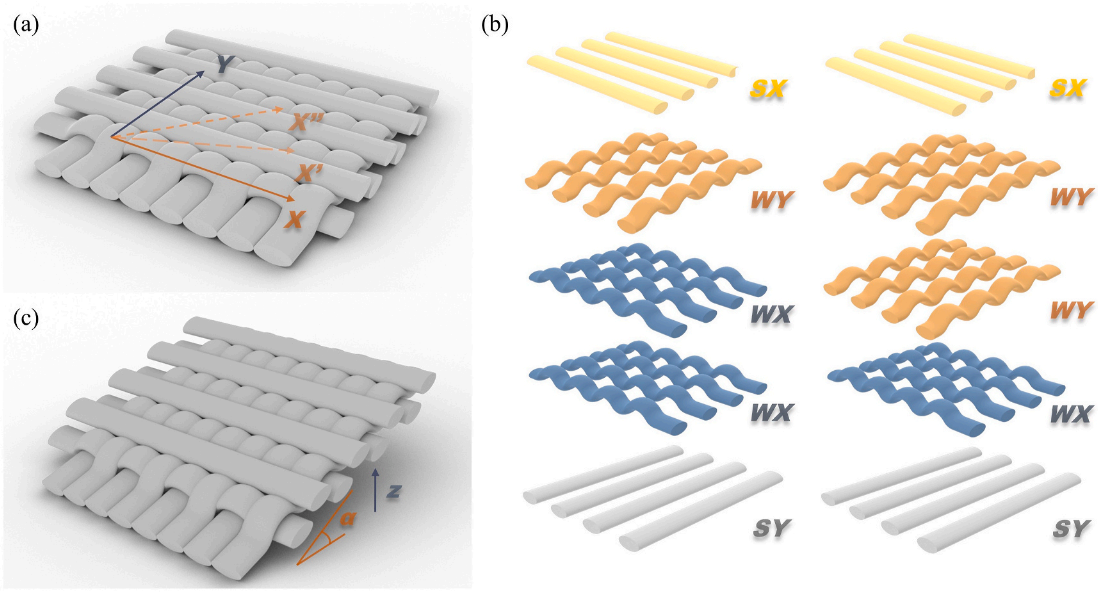

Fig. 16. Design parameters in "stitching" pattern: (a) inter-element angle, (b) sequences of basic elements, and (c) structure inclination ("tilting").

of-plane ductility and strength of 3D-printed structures. Through experimental investigation and analysis, the following primary conclusions can be drawn:

(1) The "stitching" strategy was developed based on several theoretical principles: the fiber alignment inside extruded ECC, the mechanical interlocking among interwoven layers, and the engineered complex interface system. This approach exploits the inherent properties of fiber-reinforced composites and the design flexibility offered by 3D printing, integrating an architected structural design grounded in fracture mechanics.
(2) The effectiveness of the proposed strategy was validated through four-point bending tests. The stitching strategy induced flexural hardening in ST3, promoting its energy dissipation to 343 % of the reference parallel printing, demonstrating substantial anisotropy alleviation.
(3) Micro-CT and AET analysis provided valuable insight into the failure mechanisms. The controlled crack propagation enabled by the engineered interface architecture is the primary driver of performance improvements achieved through the "stitching" strategy.
(4) The proposed strategy provides exceptional geometric adaptability, design versatility, and tunable mechanical performance, making it particularly well-suited for applications involving shells, domes, and intricately shaped components.

CRediT authorship contribution statement

Wen Zhou: Writing – original draft, Validation, Methodology, Investigation, Formal analysis, Conceptualization. **Yading Xu:** Writing – review & editing, Methodology, Investigation. **Zhaozheng Meng:** Writing – review & editing, Investigation. **Jinbao Xie:** Writing – review & editing, Investigation. **Yubao Zhou:** Writing – review & editing, Investigation, Data curation. **Erik Schlangen:** Writing – review & editing, Supervision. **Branko Šavija:** Writing – review & editing, Supervision, Funding acquisition.

Declaration of competing interest

The authors declare that they have no known competing financial interests or personal relationships that could have appeared to influence the work reported in this paper.

Acknowledgments

The financial support from the European Research Council (ERC) within the framework of the ERC Starting Grant Project "Auxetic Cementitious Composites by 3D printing (ACC-3D)", Grant Agreement Number 101041342, is acknowledged. Views and opinions expressed are however those of the authors only and do not necessarily reflect those of the European Union or the European Research Council. Neither the European Union nor the granting authority can be held responsible for them. The authors would like to acknowledge Laura Gómez Jaramillo, Coen Jansen and Maiko van Leeuwen for their assistance.

Data availability

Data will be made available on request.

References

[1] G. Ma, R. Buswell, W.R. Leal da Silva, L. Wang, J. Xu, S.Z. Jones, Technology readiness: a global snapshot of 3D concrete printing and the frontiers for development, Cement Concr. Res. 156 (2022) 106774, https://doi.org/10.1016/j.cemconres.2022.106774.
[2] F.P. Bos, C. Menna, M. Pradena, E. Kreiger, W.R.L. da Silva, A.U. Rehman, D. Weger, R.J.M. Wolfs, Y. Zhang, L. Ferrara, V. Mechtcherine, The realities of additively manufactured concrete structures in practice, Cement Concr. Res. 156 (2022) 106746, https://doi.org/10.1016/j.cemconres.2022.106746.
[3] T. Wangler, N. Roussel, F.P. Bos, T.A.M. Salet, R.J. Flatt, Digital concrete: a review, Cement Concr. Res. 123 (2019) 105780, https://doi.org/10.1016/j.cemconres.2019.105780.
[4] V.C. Li, F.P. Bos, K. Yu, W. McGee, T.Y. Ng, S.C. Figueiredo, K. Nefs, V. Mechtcherine, V.N. Nerella, J. Pan, G.P.A.G. van Zijl, P.J. Kruger, On the emergence of 3D printable engineered, strain hardening cementitious composites (ECC/SHCC), Cement Concr. Res. 132 (2020) 106038, https://doi.org/10.1016/j.cemconres.2020.106038.
[5] A. Hasani, S. Dorafshan, Transforming construction? Evaluation of the state of structural 3D concrete printing in research and practice, Constr. Build. Mater. 438 (2024) 137027, https://doi.org/10.1016/j.conbuildmat.2024.137027.
[6] T. Ding, J. Xiao, V. Mechtcherine, Microstructure and mechanical properties of interlayer regions in extrusion-based 3D printed concrete: a critical review, Cem. Concr. Compos. 141 (2023) 105154, https://doi.org/10.1016/j.cemconcomp.2023.105154.
[7] T.T. Le, S.A. Austin, S. Lim, R.A. Buswell, R. Law, A.G.F. Gibb, T. Thorpe, Hardened properties of high-performance printing concrete, Cement Concr. Res. 42 (2012) 558–566, https://doi.org/10.1016/j.cemconres.2011.12.003.
[8] E. Keita, H. Bessaies-Bey, W. Zuo, P. Belin, N. Roussel, Weak bond strength between successive layers in extrusion-based additive manufacturing:

measurement and physical origin, Cement Concr. Res. 123 (2019) 105787, https://doi.org/10.1016/j.cemconres.2019.105787.
[9] J. Van Der Putten, M. Deprez, V. Cnudde, G. De Schutter, K. Van Tittelboom, Microstructural characterization of 3D printed cementitious materials, Materials 12 (2019) 2993, https://doi.org/10.3390/ma12182993.
[10] B. Panda, S.C. Paul, N.A.N. Mohamed, Y.W.D. Tay, M.J. Tan, Measurement of tensile bond strength of 3D printed geopolymer mortar, Measurement 113 (2018) 108–116, https://doi.org/10.1016/j.measurement.2017.08.051.
[11] B. Panda, N.A. Noor Mohamed, S.C. Paul, G.V.P. Bhagath Singh, M.J. Tan, B. Šavija, The effect of material fresh properties and process parameters on buildability and interlayer adhesion of 3D printed concrete, Materials 12 (2019) 2149, https://doi.org/10.3390/ma12132149.
[12] B. Zareiyan, B. Khoshnevis, Effects of interlocking on interlayer adhesion and strength of structures in 3D printing of concrete, Autom. ConStruct. 83 (2017) 212–221, https://doi.org/10.1016/j.autcon.2017.08.019.
[13] T. Ding, J. Xiao, S. Zou, Y. Wang, Hardened properties of layered 3D printed concrete with recycled sand, Cem. Concr. Compos. 113 (2020) 103724, https://doi.org/10.1016/j.cemconcomp.2020.103724.
[14] A. Baktheer, M. Classen, A review of recent trends and challenges in numerical modeling of the anisotropic behavior of hardened 3D printed concrete, Addit. Manuf. 89 (2024) 104309, https://doi.org/10.1016/j.addma.2024.104309.
[15] R. Dilawar Riaz, M. Usman, A. Ali, U. Majid, M. Faizan, U. Jalil Malik, Inclusive characterization of 3D printed concrete (3DPC) in additive manufacturing: a detailed review, Constr. Build. Mater. 394 (2023) 132229, https://doi.org/10.1016/j.conbuildmat.2023.132229.
[16] R.J.M. Wolfs, F.P. Bos, T.A.M. Salet, Hardened properties of 3D printed concrete: the influence of process parameters on interlayer adhesion, Cement Concr. Res. 119 (2019) 132–140, https://doi.org/10.1016/j.cemconres.2019.02.017.
[17] X. Sun, J. Zhou, Q. Wang, J. Shi, H. Wang, PVA fibre reinforced high-strength cementitious composite for 3D printing: mechanical properties and durability, Addit. Manuf. 49 (2022) 102500, https://doi.org/10.1016/j.addma.2021.102500.
[18] F. Aslani, R. Dale, F. Hamidi, A. Valizadeh, Mechanical and shrinkage performance of 3D-printed rubberised engineered cementitious composites, Constr. Build. Mater. 339 (2022) 127665, https://doi.org/10.1016/j.conbuildmat.2022.127665.
[19] W. Zhou, 3D printing of engineered cementitious composites (3DP-ECC), Thesis, https://doi.org/10.7302/8326, 2023.
[20] G. Ma, Z. Li, L. Wang, F. Wang, J. Sanjayan, Mechanical anisotropy of aligned fiber reinforced composite for extrusion-based 3D printing, Constr. Build. Mater. 202 (2019) 770–783, https://doi.org/10.1016/j.conbuildmat.2019.01.008.
[21] S.B.F. Warsi, B. Panda, P. Biswas, Exploring fibre addition methods and mechanical properties of fibre-reinforced 3D printed concrete: a review, Dev. Built Environ. 16 (2023) 100295, https://doi.org/10.1016/j.dibe.2023.100295.
[22] S.B.F. Warsi, B. Panda, P. Biswas, Development of ultra-ductile strain hardening 3D printed concrete composite utilizing critical fiber volume and coarse aggregate, Addit. Manuf. 95 (2024) 104541, https://doi.org/10.1016/j.addma.2024.104541.
[23] S. Chaves Figueiredo, C. Romero Rodríguez, Z.Y. Ahmed, D.H. Bos, Y. Xu, T. M. Salet, O. Çopuroğlu, E. Schlangen, F.P. Bos, Mechanical behavior of printed strain hardening cementitious composites, Materials 13 (2020) 2253, https://doi.org/10.3390/ma13102253.
[24] M. Hambach, D. Volkmer, Properties of 3D-printed fiber-reinforced Portland cement paste, Cem. Concr. Compos. 79 (2017) 62–70, https://doi.org/10.1016/j.cemconcomp.2017.02.001.
[25] B. Zhu, J. Pan, B. Nematollahi, Z. Zhou, Y. Zhang, J. Sanjayan, Development of 3D printable engineered cementitious composites with ultra-high tensile ductility for digital construction, Mater. Des. 181 (2019) 108088, https://doi.org/10.1016/j.matdes.2019.108088.
[26] K. Yu, W. McGee, T.Y. Ng, H. Zhu, V.C. Li, 3D-printable engineered cementitious composites (3DP-ECC): fresh and hardened properties, Cement Concr. Res. 143 (2021) 106388, https://doi.org/10.1016/j.cemconres.2021.106388.
[27] N. Xu, Y. Qian, J. Yu, C.K.Y. Leung, Tensile performance of 3D-printed Strain-Hardening Cementitious Composites (SHCC) considering material parameters, nozzle size and printing pattern, Cem. Concr. Compos. 132 (2022) 104601, https://doi.org/10.1016/j.cemconcomp.2022.104601.
[28] A.R. Arunothayan, B. Nematollahi, R. Ranade, S.H. Bong, J.G. Sanjayan, K. H. Khayat, Fiber orientation effects on ultra-high performance concrete formed by 3D printing, Cement Concr. Res. 143 (2021) 106384, https://doi.org/10.1016/j.cemconres.2021.106384.
[29] W. Zhou, Y. Zhang, L. Ma, V.C. Li, Influence of printing parameters on 3D printing engineered cementitious composites (3DP-ECC), Cem. Concr. Compos. 130 (2022) 104562, https://doi.org/10.1016/j.cemconcomp.2022.104562.
[30] T. Ding, J. Xiao, S. Zou, X. Zhou, Anisotropic behavior in bending of 3D printed concrete reinforced with fibers, Compos. Struct. 254 (2020) 112808, https://doi.org/10.1016/j.compstruct.2020.112808.
[31] W. Zhou, W. McGee, H.S. Gökçe, V.C. Li, A bio-inspired solution to alleviate anisotropy of 3D printed engineered cementitious composites (3DP-ECC): knitting/tilting filaments, Autom. ConStruct. 155 (2023) 105051, https://doi.org/10.1016/j.autcon.2023.105051.
[32] Y. Yang, C. Wu, Z. Liu, H. Wang, Q. Ren, Mechanical anisotropy of ultra-high performance fibre-reinforced concrete for 3D printing, Cem. Concr. Compos. 125 (2022) 104310, https://doi.org/10.1016/j.cemconcomp.2021.104310.
[33] D. Liu, Z. Zhang, X. Zhang, Z. Chen, 3D printing concrete structures: state of the art, challenges, and opportunities, Constr. Build. Mater. 405 (2023) 133364, https://doi.org/10.1016/j.conbuildmat.2023.133364.
[34] M.T. Souza, I.M. Ferreira, E. Guzi de Moraes, L. Senff, A.P. Novaes de Oliveira, 3D printed concrete for large-scale buildings: an overview of rheology, printing parameters, chemical admixtures, reinforcements, and economic and environmental prospects, J. Build. Eng. 32 (2020) 101833, https://doi.org/10.1016/j.jobe.2020.101833.
[35] H. Kloft, B. Sawicki, F. Bos, R. Dörrie, N. Freund, S. Gantner, L. Gebhard, N. Hack, E. Ivaniuk, J. Kruger, W. Kaufmann, J. Mata-Falcón, V. Mechtcherine, A. Mirjan, R. Wolfs, D. Lowke, Interaction of reinforcement, process, and form in digital fabrication with concrete, Cement Concr. Res. 186 (2024) 107640, https://doi.org/10.1016/j.cemconres.2024.107640.
[36] A. Kamhawi, M. Aghaei Meibodi, Techniques and strategies in extrusion based 3D concrete printing of complex components to prevent premature failure, Autom. ConStruct. 168 (2024) 105768, https://doi.org/10.1016/j.autcon.2024.105768.
[37] V. Mechtcherine, R. Buswell, H. Kloft, F.P. Bos, N. Hack, R. Wolfs, J. Sanjayan, B. Nematollahi, E. Ivaniuk, T. Neef, Integrating reinforcement in digital fabrication with concrete: a review and classification framework, Cem. Concr. Compos. 119 (2021) 103964, https://doi.org/10.1016/j.cemconcomp.2021.103964.
[38] S. Kristombu Baduge, S. Navaratnam, Y. Abu-Zidan, T. McCormack, K. Nguyen, P. Mendis, G. Zhang, L. Aye, Improving performance of additive manufactured (3D printed) concrete: a review on material mix design, processing, interlayer bonding, and reinforcing methods, Structures 29 (2021) 1597–1609, https://doi.org/10.1016/j.istruc.2020.12.061.
[39] L. Hass, K. Nefs, F.P. Bos, T.A.M. Salet, Application potential of combining strain hardening cementitious composites and helical reinforcement for 3D concrete printed structures: case study of a spiral staircase, J. Build. Eng. 80 (2023) 107926, https://doi.org/10.1016/j.jobe.2023.107926.
[40] L. Hass, F.P. Bos, T.A.M. Salet, Bond governed interactions between helical reinforcement and 3D printed concrete, J. Build. Eng. (2024) 111447, https://doi.org/10.1016/j.jobe.2024.111447.
[41] L. Hass, F.P. Bos, T.A.M. Salet, Characterizing the bond properties of automatically placed helical reinforcement in 3D printed concrete, Constr. Build. Mater. 355 (2022) 129228, https://doi.org/10.1016/j.conbuildmat.2022.129228.
[42] T. Marchment, J. Sanjayan, Reinforcement method for 3D concrete printing using paste-coated bar penetrations, Autom. ConStruct. 127 (2021) 103694, https://doi.org/10.1016/j.autcon.2021.103694.
[43] V. Mechtcherine, J. Grafe, V.N. Nerella, E. Spaniol, M. Hertel, U. Füssel, 3D-printed steel reinforcement for digital concrete construction – manufacture, mechanical properties and bond behaviour, Constr. Build. Mater. 179 (2018) 125–137, https://doi.org/10.1016/j.conbuildmat.2018.05.202.
[44] F. Bester, J. Kruger, G. van Zijl, Rivet reinforcement for concrete printing, Addit. Manuf. 67 (2023) 103490, https://doi.org/10.1016/j.addma.2023.103490.
[45] A. Ramesh, P. Rajeev, J. Sanjayan, Bond-slip behaviour of textile-reinforcement in 3D printed concrete, J. Build. Eng. 86 (2024) 108873, https://doi.org/10.1016/j.jobe.2024.108873.
[46] A. Ramesh, P. Rajeev, J. Sanjayan, V. Mechtcherine, In-process textile reinforcement method for 3D concrete printing and its structural performance, Eng. Struct. 314 (2024) 118337, https://doi.org/10.1016/j.engstruct.2024.118337.
[47] T. Marchment, J. Sanjayan, Mesh reinforcing method for 3D concrete printing, Autom. ConStruct. 109 (2020) 102992, https://doi.org/10.1016/j.autcon.2019.102992.
[48] J. Cao, E. Shengzhao, Y. Yang, Y. Shi, J. Chai, Z. Xu, A strategy for the improvement of the bonding performance of 3D-printed concrete interlayer interfaces, J. Build. Eng. 97 (2024) 110675, https://doi.org/10.1016/j.jobe.2024.110675.
[49] X. Feng, G. Du, V. Carvelli, G. Lin, D. Pan, P. Huang, C. Zhu, Failure analysis of 3D concrete printing bolted laminates mimicking geological strata, Eng. Fail. Anal. 163 (2024) 108463, https://doi.org/10.1016/j.engfailanal.2024.108463.
[50] C. Liu, Y. Zhang, H. Liu, Y. Wu, S. Yu, C. He, Z. Liang, Interlayer reinforced 3D printed concrete with recycled coarse aggregate: shear properties and enhancement methods, Addit. Manuf. 94 (2024) 104507, https://doi.org/10.1016/j.addma.2024.104507.
[51] L. Wang, G. Ma, T. Liu, R. Buswell, Z. Li, Interlayer reinforcement of 3D printed concrete by the in-process deposition of U-nails, Cement Concr. Res. 148 (2021) 106535, https://doi.org/10.1016/j.cemconres.2021.106535.
[52] T. Marchment, J. Sanjayan, M. Xia, Method of enhancing interlayer bond strength in construction scale 3D printing with mortar by effective bond area amplification, Mater. Des. 169 (2019) 107684, https://doi.org/10.1016/j.matdes.2019.107684.
[53] G. Ma, N.M. Salman, L. Wang, F. Wang, A novel additive mortar leveraging internal curing for enhancing interlayer bonding of cementitious composite for 3D printing, Constr. Build. Mater. 244 (2020) 118305, https://doi.org/10.1016/j.conbuildmat.2020.118305.
[54] E. Hosseini, M. Zakertabrizi, A. Habibnejad Korayem, Z. Zaker, R. Shahsavari, Orbital overlapping through induction bonding overcomes the intrinsic delamination of 3D-printed cementitious binders, ACS Nano 14 (2020) 9466–9477, https://doi.org/10.1021/acsnano.0c02038.
[55] Y. Weng, M. Li, T.N. Wong, M.J. Tan, Synchronized concrete and bonding agent deposition system for interlayer bond strength enhancement in 3D concrete printing, Autom. ConStruct. 123 (2021) 103546, https://doi.org/10.1016/j.autcon.2020.103546.
[56] E. Hosseini, M. Zakertabrizi, A.H. Korayem, G. Xu, A novel method to enhance the interlayer bonding of 3D printing concrete: an experimental and computational investigation, Cem. Concr. Compos. 99 (2019) 112–119, https://doi.org/10.1016/j.cemconcomp.2019.03.008.
[57] F. Teng, J. Ye, J. Yu, H. Li, Y. Weng, V. Mechtcherine, Development of strain-hardening cementitious composites (SHCC) as bonding materials to enhance interlayer and flexural performance of 3D printed concrete, Cem. Concr. Compos. 152 (2024) 105657, https://doi.org/10.1016/j.cemconcomp.2024.105657.

[58] J. Guan, L. Wang, Y. Huang, G. Ma, 3D printed concrete composite slabs fabricated by prestress reinforced permanent formwork: design, manufacturing, and performance, Eng. Struct. 325 (2025) 119446, https://doi.org/10.1016/j.engstruct.2024.119446.
[59] G. Vantyghem, W. De Corte, E. Shakour, O. Amir, 3D printing of a post-tensioned concrete girder designed by topology optimization, Autom. ConStruct. 112 (2020) 103084, https://doi.org/10.1016/j.autcon.2020.103084.
[60] Y. Li, H. Wu, X. Xie, L. Zhang, P.F. Yuan, Y.M. Xie, FloatArch: a cable-supported, unreinforced, and re-assemblable 3D-printed concrete structure designed using multi-material topology optimization, Addit. Manuf. 81 (2024) 104012, https://doi.org/10.1016/j.addma.2024.104012.
[61] L. Gebhard, J. Mata-Falcón, A. Iqbal, W. Kaufmann, Structural behaviour of post-installed reinforcement for 3D concrete printed shells – a case study on water tanks, Constr. Build. Mater. 366 (2023) 130163, https://doi.org/10.1016/j.conbuildmat.2022.130163.
[62] T.A.M. Salet, Z.Y. Ahmed, F.P. Bos, H.L.M. Laagland, Design of a 3D printed concrete bridge by testing, Virtual Phys. Prototyp. 13 (2018) 222–236, https://doi.org/10.1080/17452759.2018.1476064.
[63] A. Aramburu, I. Calderon-Uriszar-Aldaca, I. Puente, Bonding strength of steel rebars perpendicular to the hardened 3D-printed concrete layers, Constr. Build. Mater. 340 (2022) 127827, https://doi.org/10.1016/j.conbuildmat.2022.127827.
[64] M. Classen, J. Ungermann, R. Sharma, Additive manufacturing of reinforced concrete—development of a 3D printing technology for cementitious composites with metallic reinforcement, Appl. Sci. 10 (2020) 3791, https://doi.org/10.3390/app10113791.
[65] S. Kamat, X. Su, R. Ballarini, A.H. Heuer, Structural basis for the fracture toughness of the shell of the conch Strombus gigas, Nature 405 (2000) 1036–1040, https://doi.org/10.1038/35016535.
[66] L.T. Kuhn-Spearing, H. Kessler, E. Chateau, R. Ballarini, A.H. Heuer, S.M. Spearing, Fracture mechanisms of the Strombus gigas conch shell: implications for the design of brittle laminates, J. Mater. Sci. 31 (1996) 6583–6594, https://doi.org/10.1007/BF00356266.
[67] W. Huang, D. Restrepo, J.-Y. Jung, F.Y. Su, Z. Liu, R.O. Ritchie, J. McKittrick, P. Zavattieri, D. Kisailus, Multiscale toughening mechanisms in biological materials and bioinspired designs, Adv. Mater. 31 (2019) 1901561, https://doi.org/10.1002/adma.201901561.
[68] Y. Zhang, O. Paris, N.J. Terrill, H.S. Gupta, Uncovering three-dimensional gradients in fibrillar orientation in an impact-resistant biological armour, Sci. Rep. 6 (2016) 26249, https://doi.org/10.1038/srep26249.
[69] S. Gupta, H.S. Esmaeeli, R. Moini, Tough and ductile architected nacre-like cementitious composites (adv. Funct. Mater. 39/2024), Adv. Funct. Mater. 34 (2024) 2470230, https://doi.org/10.1002/adfm.202470230.
[70] J. Liu, S. Li, K. Fox, P. Tran, 3D concrete printing of bioinspired Bouligand structure: a study on impact resistance, Addit. Manuf. 50 (2022) 102544, https://doi.org/10.1016/j.addma.2021.102544.
[71] A. Prihar, S. Gupta, H.S. Esmaeeli, R. Moini, Tough double-bouligand architected concrete enabled by robotic additive manufacturing, Nat. Commun. 15 (2024) 7498, https://doi.org/10.1038/s41467-024-51640-y.
[72] A.A. Griffith, VI. The phenomena of rupture and flow in solids, Philos. Trans. R. Soc. Lond. - Ser. A Contain. Pap. a Math. or Phys. Character 221 (1921) 163–198, https://doi.org/10.1098/rsta.1921.0006.
[73] Y.M. Lim, V.C. Li, Durable repair of aged infrastructures using trapping mechanism of engineered cementitious composites, Cem. Concr. Compos. 19 (1997) 373–385, https://doi.org/10.1016/S0958-9465(97)00026-7.
[74] P.M. Pohl, F. Kümmel, C. Schunk, I. Serrano-Munoz, H. Markötter, M. Göken, H. W. Höppel, About the role of interfaces on the fatigue crack propagation in laminated metallic composites, Materials 14 (2021) 2564, https://doi.org/10.3390/ma14102564.
[75] V. Tvergaard, J.W. Hutchinson, The relation between crack growth resistance and fracture process parameters in elastic-plastic solids, J. Mech. Phys. Solid. 40 (1992) 1377–1397, https://doi.org/10.1016/0022-5096(92)90020-3.
[76] Y. Jiao, Y. Zhang, W. Shan, Q. Han, Y. Zhao, S. Liu, Damage fracture characterization of reinforced concrete beam subjected to four-point bending with parametric analysis of static, dynamic, and acoustic properties, Struct. Health Monit. 19 (2020) 1202–1218, https://doi.org/10.1177/1475921719881756.
[77] Y. Zhou, M. Liang, X. Yue, Deep residual learning for acoustic emission source localization in A steel-concrete composite slab, Constr. Build. Mater. 411 (2024) 134220, https://doi.org/10.1016/j.conbuildmat.2023.134220.
[78] N. Holsamudrkar, S. Banerjee, Acoustic Emission (AE) based health monitoring of RC beams strengthened with mechanically anchored hybrid Fiber Reinforced Cementitious Matrix (FRCM) system, Case Stud. Constr. Mater. 21 (2024) e03773, https://doi.org/10.1016/j.cscm.2024.e03773.
[79] Z. Chen, G. Zhang, R. He, Z. Tian, C. Fu, X. Jin, Acoustic emission analysis of crack type identification of corroded concrete columns under eccentric loading: a comparative analysis of RA-AF method and Gaussian mixture model, Case Stud. Constr. Mater. 18 (2023) e02021, https://doi.org/10.1016/j.cscm.2023.e02021.
[80] D.D. Mandal, M. Bentahar, A. El Mahi, A. Brouste, R. El Guerjouma, S. Montresor, F.-B. Cartiaux, Acoustic emission monitoring of progressive damage of reinforced concrete T-beams under four-point bending, Materials 15 (2022) 3486, https://doi.org/10.3390/ma15103486.
[81] J. Chang, Y. Yao, K. Liu, Y. Wang, M. Yan, Y. Bao, Damage assessment of concrete beams repaired with basalt fiber-reinforced polymer sheets through digital image correlation and acoustic emission, Case Stud. Constr. Mater. 20 (2024) e03044, https://doi.org/10.1016/j.cscm.2024.e03044.